



In-situ transformation into MoSe₂/MoO₃ heterogeneous nanostructures with enhanced electrochemical performance as anode material for sodium ion battery



Wenpei Kang*, Yuyu Wang, Dongwei Cao, Zixi Kang, Daofeng Sun**

College of Science, China University of Petroleum (East China), Qingdao, Shandong, 266580, PR China

ARTICLE INFO

Article history:

Received 25 December 2017
Received in revised form
2 February 2018
Accepted 4 February 2018
Available online 5 February 2018

Keywords:

MoSe₂/MoO₃ composite
Sodium ion batteries
Anode materials
High performance

ABSTRACT

As anode materials, the electrochemical performance of layered transition metal dichalcogenides (TMDs), can be improved with surface layer protection. In this study, flower-like MoSe₂ nanostructures are easily obtained from a solvothermal reaction followed by an annealed process in inert atmosphere. Then the MoSe₂ nanostructures are further treated in air at 350 °C, and amorphous MoO₃ can be formed on MoSe₂ surfaces, resulting into MoSe₂/MoO₃ heterogeneous nanostructures. The MoSe₂/MoO₃ composite, as anode materials for sodium ion batteries (SIBs), shows better performance than those of pristine MoSe₂, which includes charge/discharge capacity, cycling stability and rate capability. At low current of 50 mA g⁻¹, the discharge capacity can reach as high as 729 mAh g⁻¹. In addition, even at high current of 10 A g⁻¹, the discharge capacity maintains at 314 mAh g⁻¹. At high currents of 1000 and 2000 mA g⁻¹, after 200 cycles, the capacity retention can be kept at 101.9% and 99.5%, respectively. The enhanced performance of MoSe₂/MoO₃ heterogeneous nanostructures can be attributed to the amorphous MoO₃ surface layer, which prevents selenium dissolution and subsequently improves the cycle performance and increases sodiation/desodiation kinetics because of the amorphous nature.

© 2018 Elsevier B.V. All rights reserved.

1. Introduction

Recently, large amount of attention has been focused on the development for decent renewable and sustainable resources (e.g., solar or wind) and its energy storage field, to relieve the increasing environmental problems and energy crisis originating from the use of traditional fossil fuel [1]. Under the considering of the practical, resource and economic issues, sodium ion batteries (SIBs) have been recommended as a promising alternative to conventional lithium ion batteries (LIBs), which is attributed to their analogous structure and electrochemistry behaviors [2–4]. During the past 5 years, many efforts have been devoted to the development of low-cost and high-performance SIBs to utilize the abundant and easily accessible Na resources [5]. However, the sodiation/desodiation kinetics are difficult partly due to the fact that the radius of Na⁺ ion (~0.98 Å) is larger than that of Li⁺ ion (~0.69 Å) [6]. Plenty of cathodes [7–10], anodes [11–13] and electrolytes [14,15] have been

intensely explored in order to improve the electrochemical performance of SIBs.

Generally, the anodes determine some key characteristics in secondary batteries, such as safety and cycling life. Therefore, it is urgent to develop suitable anode materials with fast sodiation/desodiation kinetics and high charge/discharge capacities. Graphite materials, as commercial LIB anode materials, suffer from poor insertion/extraction kinetics with Na⁺ ions due to the low insertion voltage [16]. Alternative anode for the SIBs, such as nongraphitic carbon [17,18], metal alloys (e.g., Sn, Sb, P) [14,15,19–21], intercalation compounds [22,23], and conversion reaction based metal compounds [24–31], have been widely studied for improving the electrochemical performance. Among them, the layered transition metal dichalcogenides (TMDs) proved to be good potential SIB anodes due to their specific layered structures with large interlayer spacings [32–34]. Layered MoSe₂ formed by weak van der Waals between covalently bonded (Se-Mo-Se) monolayers, has a similar sandwich structure and energy storage mechanism to MoS₂, delivering theoretic capacity of 422 mAh g⁻¹ according to the reaction between one MoSe₂ molecule and four Na⁺ ions [26,35]. The layer spacing (0.646 nm) is larger than that of MoS₂ or graphite. As a

* Corresponding author.

** Corresponding author.

E-mail addresses: wpkang@upc.edu.cn (W. Kang), dfsun@upc.edu.cn (D. Sun).

result, much faster sodiation/desodiation kinetics is expected from the MoSe₂ anode in SIBs.

Previous studies indicated that MoSe₂ is a promising SIB anode alternative [11]. Similar to other TMD anode, the modification with carbon-based materials for MoSe₂ has been considered as an effective method to enhance its sodium storage performance [36–40]. However, the sulfur/selenium dissolution originating from soluble polysulfide/polyseleminate intermediates during the formation/decomposition process of Na₂S/Na₂Se, should attract our attention, as it may worsen the electrochemical performance of TMD anodes. Based on the success of Li-S or Li-Se batteries, protective layer on the surface of TMDs could enhance the cyclability by preventing the intermediate dissolution and sulfur/selenium phase accumulation on the counter electrode [41–45]. Surface protection has been used for MoS₂ and WS₂ anodes in SIBs and the cyclic performance was significantly improved [46,47]. Alshareef et al. reported coating MoS₂ nanosheets with a nanoscale layer of HfO₂ to form a MoS₂/HfO₂ composite. As anode material for SIBs, the cyclic performance was tremendously improved, the MoS₂/HfO₂ electrode was able to retain 91% of its second discharge capacity after 50-cycles [46]. Compared to the pristine WS_x and WO₃ nanofibers, the heterogeneous WS_x/WO₃ nanofiber anode delivered a high second discharge capacity of 791 mAh g⁻¹ and improved cycle performance for 100 cycles [47]. Hence, the surface protective layer on the TMD anode can effectively enhance the electrochemical performance.

In this work, heterogeneous MoSe₂/MoO₃ nanostructure composite were studied as an improved SIB anode. Layered MoSe₂ nanoflowers were prepared through a facile solvothermal reaction followed by high-temperature annealing in an inert atmosphere. Post-thermal treatment in air was performed to form an oxide coating on the surfaces of MoSe₂ nanostructure, resulting in the MoSe₂/MoO₃ heterogeneous nanostructure composite. As an anode material for SIBs, the rate capability and cycling performance are enhanced remarkably.

2. Experimental

2.1. MoSe₂ and MoSe₂/MoO₃ composite synthesis

MoSe₂ was prepared using a solvothermal reaction. In a typical process, 0.5 mmol molybdophosphoric acid and 1.0 mmol selenium dioxide were added into a mixed solvent (25.0 mL octylamine and 5.0 mL ethanol) and stirred for 12 h to form a transparent solution. The above solution was transferred into a Teflon-lined stainless steel autoclave and maintained at 200 °C for 24 h. After cooling to room temperature naturally, the obtained black precipitate was collected by centrifugation, washed with absolute ethanol several times, and dried at 80 °C for 12 h. The as-prepared MoSe₂ sample was calcined at 700 °C for 3 h in a mixed Ar-H₂ (5% H₂) atmosphere with a heating rate of 10 °C/min. In order to obtain the *in-situ* oxide layer, when the muffle furnace increased to 350 °C, the calcined MoSe₂ was put into it and maintained for 10 min in air atmosphere. After the post-thermal treatment, MoSe₂/MoO₃ composite was obtained.

2.2. Material characterization

The crystal structure of the samples was examined by means of X-ray diffraction (XRD, Ultima IV, Cu K α radiation). Raman measurements were performed on a HORIBA Evolution laser Raman microscope (532 nm argon ion laser). X-ray photoelectron spectroscopy (XPS) analysis was performed with a Thermo ESCALAB 250 surface analysis system. Scanning electron microscopy (SEM) was carried out with a Philips XL30 FEG SEM. Transmission electron

microscopy (TEM) was carried out with a JEOL JEM-2100 TEM operated at 200 kV. thermogravimetric analysis (TGA) was carried out on Mettler Toledo TGA-DSC 1 in an air atmosphere.

2.3. Electrochemical measurements

Working electrodes were prepared by coating slurries of active material mixed with acetylene black and sodium carboxymethyl cellulose at a weight ratio of 6: 2: 2 on the copper foils. The coated foils were dried at 80 °C, and then punched into discs with 12 mm diameter. The electrode discs were dried at 100 °C for 10 h and then transferred into an Ar-filled glove box. Sodium metal and glass microfiber (Whatman, GF/A) were used as counter electrode and separator, respectively. NaClO₄ (1.0 mol L⁻¹) in propylene carbonate with 5% fluoroethylene carbonate (FEC) was used as the electrolyte. Neware-5V10 mA or Neware-5V20 mA system (Shenzhen Xinwei) was used for Galvanostatic cycling tests at room temperature. Cyclic voltammetry (CV) measurements were carried out on the electrochemical workstation (Gamary reference 3000) over a potential window of 0.0–3.0 V at a scan rate of 0.1 mV s⁻¹. Electrochemical impedance spectroscopy (EIS) measurements were carried out on Gamary electrochemical workstation over a frequency range of 100 kHz to 10 mHz.

3. Results and discussion

The preparation process of heterogeneous MoSe₂/MoO₃ nanostructure is schematically illustrated in Fig. 1. After a facile solvothermal reaction followed by an annealed process in inert atmosphere, in order to partial *in-situ* transformation into MoO₃, a post-thermal treatment was performed in air at 350 °C for a short time. X-ray diffraction (XRD) patterns used to identify the crystal structure and phase purity are shown in Fig. 2a. After calcination in a mixed Ar-H₂ atmosphere, the diffraction peaks are sharp and intensive (black), indicating high crystallinity. All peaks are well indexed to hexagonal phase 2H-MoSe₂ (JCPDF 29-0914). There is no observable impurity in the annealed MoSe₂ sample. After post-thermal treatment in air at 350 °C, all diffraction peaks for MoSe₂ still existed and they became slightly weak (red). However, another weaker and broader peak appeared between 20° and 30°, suggesting amorphous oxide layer formed on the surface of the MoSe₂ [48].

The Raman spectra of MoSe₂ nanostructures and MoSe₂/MoO₃ nano-composite are shown in Fig. 2b. A strong peak is observed at 241 cm⁻¹, corresponding to the A_{1g} mode originating from the out-of-plane vibration of the Mo-Se band. Another weak peak is observed at 281 cm⁻¹, corresponding to the E¹_{2g} (Mo-Se) mode originating from the Mo-Se in-plane vibration [26]. These two typical peaks indicate the formation of MoSe₂ with high crystallinity. There are also two broad bands at approximately 1370 and 1575 cm⁻¹, corresponding to the disorder-induced D-band and the graphitic G-band of the amorphous carbon, respectively [28]. This suggested that the adsorbed octylamine molecules in the solvothermal reaction can be carbonized in the annealed process. For the composite, the peaks at 992 and 816 cm⁻¹ are the characteristics of α -MoO₃, indicating the formation of MoO₃ after post-thermal treatment in the air. The intense peak at 816 cm⁻¹ is attributed to the doubly coordinated oxygen (Mo₂O) stretching mode, resulting from the corner-shared oxygen. The peak at 992 cm⁻¹ is basically assigned to the terminal oxygen (Mo⁶⁺=O) stretching mode along the a and b directions resulting from unshared oxygen, which is also responsible for the layered structure of α -MoO₃ [48]. The XRD and Raman analysis indicate amorphous MoO₃ layer can be formed after heat-treatment in the air, resulting into the MoSe₂/MoO₃ heterogeneous composite. The TGA of the

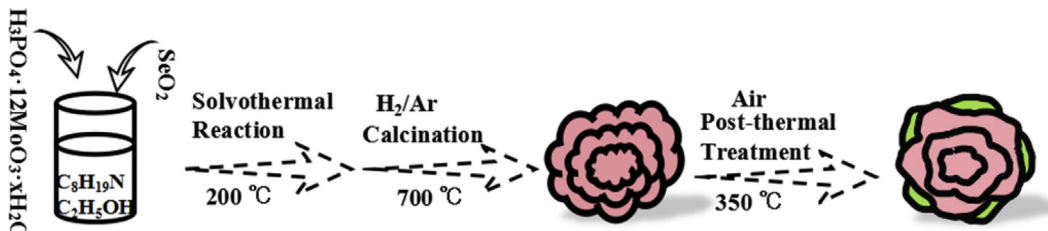


Fig. 1. Schematic diagram of the preparation of heterogeneous MoSe₂/MoO₃ nanostructure.

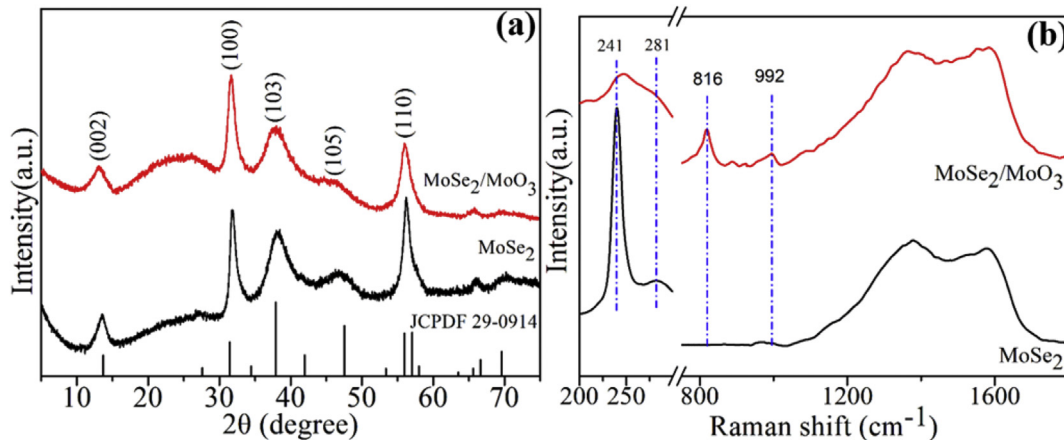


Fig. 2. (a) XRD and (b) Raman spectra of MoSe₂ nanostructure and MoSe₂/MoO₃ composite.

two samples was performed and compared as shown in Fig. 3. The weight increased above 255 °C attributed to the formation of SeO₂. Between 300 °C and 400 °C the weight dramatically decrease due to the oxidation of the doped C and MoSe₂. In order to obtain an MoO₃ layer, we chose the post-heat treatment temperature to be 350 °C. The weight increase of MoSe₂/MoO₃ composite (14.0%) above 255 °C is lower than that of MoSe₂ nanostructure (18.0%). This further proved the partial oxidation of MoSe₂ into MoO₃ for the MoSe₂/MoO₃ composite. And the weight loss is almost the same for the two samples, indicating the doped C was maintained after post-heat treatment in air, which is in accordance with the result of

the Raman results.

Oxidation states and surface information of the chemical elements in the two samples were investigated using XPS, as shown in Fig. 4. A survey spectrum (Fig. 4a) shows the presence of Mo, Se, O, C and N elements. The Mo core level XPS spectrum is shown in Fig. 4b, with peaks at 232.2 eV for Mo 3d_{3/2} and 229.0 eV for Mo 3d_{5/2}, which are attributed to the Mo-Se bond in the MoSe₂ [26]. Two other characteristic peaks at 236.0 and 233.0 eV are attributed to the Mo 3d_{3/2} and Mo 3d_{5/2} for Mo⁶⁺ in the MoO₃ oxide layer, respectively [49]. In the Se core level XPS spectrum (Fig. 4c), two distinct peaks are recognized at 55.4 eV for Se 3d_{3/2} and 54.6 eV for Se 3p_{5/2}, indicating that the selenium exists as Se²⁻ ions [26]. And a weak peak at 59.2 eV corresponds to the Se-O bond, which may have formed by post-thermal treatment in air [50]. The deconvolution of O 1s peaks shows two contributions of oxygen (Fig. 4d). The lower binding energy of 530.7 eV is assigned to Mo-O in the MoO₃ and the higher bonding energy of 532.7 eV corresponds to the surface adsorbed oxygen O [49]. Fig. 4e shows the C1s spectrum, which can be divided into three peaks. The peaks at 284.8, 285.2 and 285.6 eV can be assigned respectively to the C-C, C=C and C-N bonds [26,27]. This further proves the existence of carbon originated from the carbonization of the octylamine molecules. The N core level spectrum is shown in Fig. 4f. A prominent peak at 394.7 eV corresponds to the Mo 3p_{3/2}. There are broad signals, which can be fitted into three peaks. The peak at 398.0 eV corresponds to the nitride-type of N atoms, indicating formation of N-Mo bond. The peak centered at 399.6 eV can be assigned to N atoms in the C-N bond for pyrrolic and/or pyridinic N atoms in the carbon. The peak at 401.8 eV is attributed to amino N atoms [26,27]. The XPS analysis further proves that the MoO₃ layer indeed formed on the MoSe₂ surface and N doped C can be *in-situ* formed in the high temperature annealed process. As for the MoSe₂ nanostructure, there is no O element information can be detected.

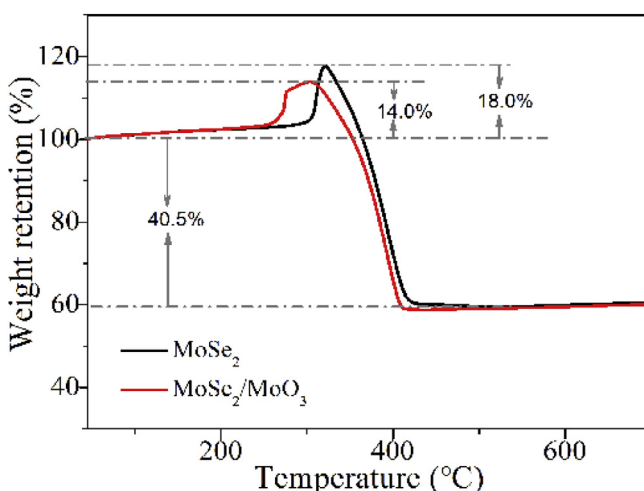


Fig. 3. TGA curves of the MoSe₂ nanostructure and MoSe₂/MoO₃ composite measured in air.

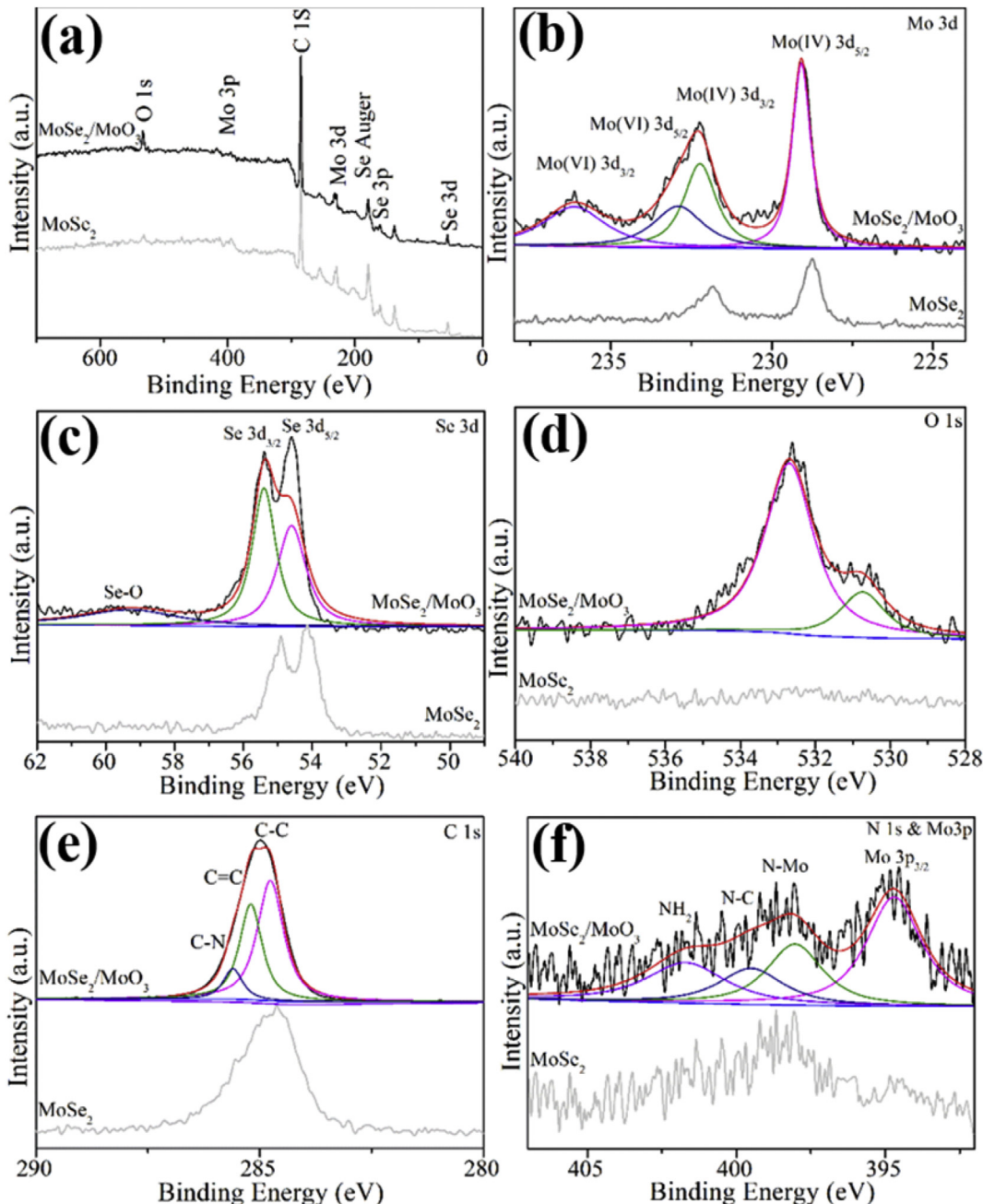


Fig. 4. XPS spectra of the $\text{MoSe}_2/\text{MoO}_3$ composite: (a) a survey spectrum, (b) Mo 3d, (c) Se 3d, (d) O 1s, (e) C 1s, and (f) N 1s & Mo 3p core level spectra.

Fig. 5 shows SEM images of the MoSe_2 and $\text{MoSe}_2/\text{MoO}_3$ composite. MoSe_2 shows a homogeneous morphology of flower-like assemblies with a size of 200–300 nm (**Fig. 5a** and b). From the magnified SEM images (**Fig. 5b**), it can be seen that the flower-like structures are assembled by the nanosheets. After heat-treatment in air, $\text{MoSe}_2/\text{MoO}_3$ also exhibits the mono-dispersed structures (**Fig. 5c**). The surfaces of the flower-like structures are slightly broken (**Fig. 5d**). The nanosheets are hardly observed in the assembled structures. As a result, the flower-like structures evolved to sphere-like structures. This indicates the heat-treatment in air can affect both the composition and morphology.

The microstructure of $\text{MoSe}_2/\text{MoO}_3$ composite was further measured by TEM and HRTEM, as shown in **Fig. 6**. The sphere structure can be observed (**Fig. 6a** and **Fig. S1**) in the TEM images,

From the TEM images, it can be concluded that the sphere structures are also assembled by the nanosheets. Different with $\text{MoSe}_2/\text{MoO}_3$ sphere structures, the flower-like structure is obvious for the MoSe_2 sample (**Fig. S2**). The layered structure can be seen in the magnified TEM images (**Fig. 6b**). The interlayer spacing is 0.65 nm (**Fig. 6c**), which corresponds to a (002) interlayer distance of MoSe_2 . The amorphous MoO_3 layer surround with MoSe_2 can be observed as marked by the blue curve in **Fig. 6c**. In addition, the selected area electron diffraction (SAED) pattern (**Fig. 6d**) shows the polycrystalline nature of the detected MoSe_2 . The diffraction ring intensity of $\text{MoSe}_2/\text{MoO}_3$ in the SAED is weaker than that of the MoSe_2 sample (**Fig. S2d**), indicating the MoO_3 formation is along with the crystallinity of MoSe_2 disrupting, which is agreement with the XRD result (**Fig. 2a**). The energy dispersive X-Ray spectroscopy

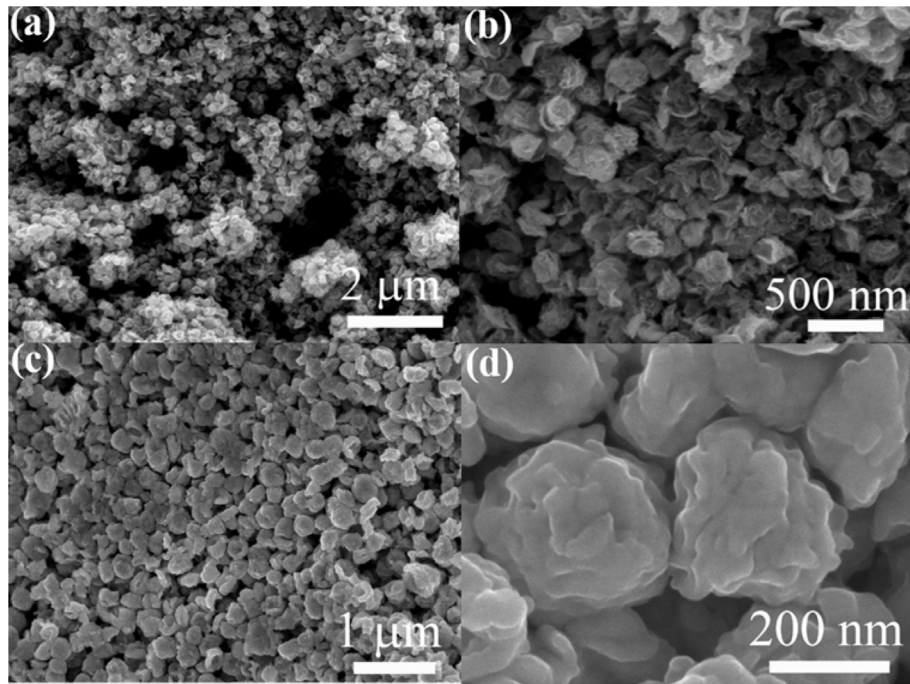


Fig. 5. SEM images of (a, b) MoSe₂ and (c, d) MoSe₂/MoO₃ composite, respectively.

(EDX) mapping shows that the composite includes these five Mo, Se, O, C and N elements and they are uniformly distributed throughout the particles (Fig. 6e).

The electrochemical performance of MoSe₂/MoO₃ composite as SIB anode material was investigated and compared with that of MoSe₂. Fig. 7a shows the CV curves of the MoSe₂/MoO₃ anode in a voltage range of 0–3.0 V vs. Na/Na⁺ at a scan rate of 0.1 mV s⁻¹ for the five initial cycles. These CV profiles are quite similar to those of the reported Mo-based anodes for SIBs [36–40]. The peak located between 1.75 V and 1.17 V correspond to the sodium insertion reaction of the MoSe₂/MoO₃ to form Na_xMoSe₂/Na_yMoO₃ [26,51]. The peak around 0.64 V is attributed to the irreversible decomposition of the electrolyte that forms a stable and thin solid-electrolyte-interface (SEI) layer, which results from the addition of the FEC additive in the electrolyte [37]. In the deep cathodic step, the main cathodic peaks are observed at around 0.44 and a tail band below 0.22 V are attributed to the decomposition of the Na_xMoSe₂/Na_yMoO₃ to metallic Mo and Na₂Se and Na₂O through a further Na⁺ ion insertion process [26,51]. In the following cathodic cycles, the strong peaks at 0.44 and 0.22 V disappeared, and both peaks based on the sodium insertion reaction and the tail band moved to higher potential because of the activation process in the first cycle. The peak intensity that corresponds to the sodium insertion reaction for the MoSe₂/MoO₃ anode is stronger than that for the MoSe₂ electrode as shown in Fig. S3. This suggests that the amorphous MoO₃ layer on the MoSe₂ surface can enhance the sodium insertion reaction because of the isotropic nature, percolation pathways and absence of grain boundaries in amorphous materials [52]. In the first anodic sweep, a major peak is observed at 1.72 V with a shoulder peak, corresponding to the reaction of the Mo metal oxidation and the inverse formation of MoSe₂/MoO₃. After the first cathodic and anodic processes, the peaks in the following cycles almost overlap, suggesting that the reversibility of Na⁺ insertion/desertion for the MoSe₂/MoO₃ composite anode is high. It indicates that the cycling performance of the composite anode is good.

Fig. 7b shows the typical discharge/charge profiles of MoSe₂/MoO₃ composite anode. A slope in the range of 1.8–0.9 V, a plateau

at 0.8–0.5 V as well as a slope below 0.4 V is observed for the initial discharge profile. The curves can be divided into two slopes at 2.0–1.2 V and below 1.0 V in the subsequent discharge curves, which are shifted to high voltage. The slope or plateau is corresponding to the peaks in the CV curves. It can be concluded that the change trend in the discharge profiles agrees well with the CV results. All charge curves exhibit obvious slopes at 1.5–2.5 V, matching well with the broad oxidation peak centered at 1.72 V in the CV curves shown in Fig. 7a. The discharge/charge profiles of the MoSe₂ anode show similar change trend as shown in Fig. S4. At the current density of 50 mA g⁻¹, the MoSe₂/MoO₃ electrode delivers an initial discharge capacity of 729 mAh g⁻¹ and a charge capacity of 530 mAh g⁻¹ with a first Coulombic efficiency (CE) of 72.7%. The irreversible capacity loss is mainly due to the formation of a SEI layer during the initial sodiation process [28]. For the MoSe₂ anode, it only delivers a lower discharge capacity of 580 mAh g⁻¹ and a slightly higher first CE of 78%. This suggest amorphous MoO₃ layer can enhance the sodium storage capability and bring more side reaction based on the formation of a stable SEI layer and extra Na⁺ adsorption on the SEI corresponding to interfacial storage [51]. Starting from the second cycle, the discharge/charge profiles are almost identical even after 200 cycles. The reversible discharge capacities for the 2nd, 10th, 50th, 100th and 200th cycles are respectively 533, 508, 522, 531, and 529 mAh g⁻¹ with CEs up to ~99%, revealing the outstanding cycling stability of MoSe₂/MoO₃ electrode. Furthermore, the electrochemical kinetics MoSe₂/MoO₃ composite anode were investigated by CV at varying scan rates (Fig. 7c). The capacitive contribution at a fixed scan rate can be quantified into the capacitive and diffusion-controlled charge storage. At a fixed potential, the contributions from the two mechanisms can be estimated from the formula $i(V) = k_1v + k_2v^{1/2}$ [52]. As shown in the inset of Fig. 7c, 67.7% of the total capacity is attributed to the capacitive contribution at a scan rate of 0.1 mV s⁻¹. As the sweep rate increased, the capacitance contribution gradually increases and reaches a value of 90.5% at 1.0 mV s⁻¹ (Fig. 7d). As a result, the high proportion of the capacitive contribution promotes the rate performance of MoSe₂/MoO₃ composite electrode.

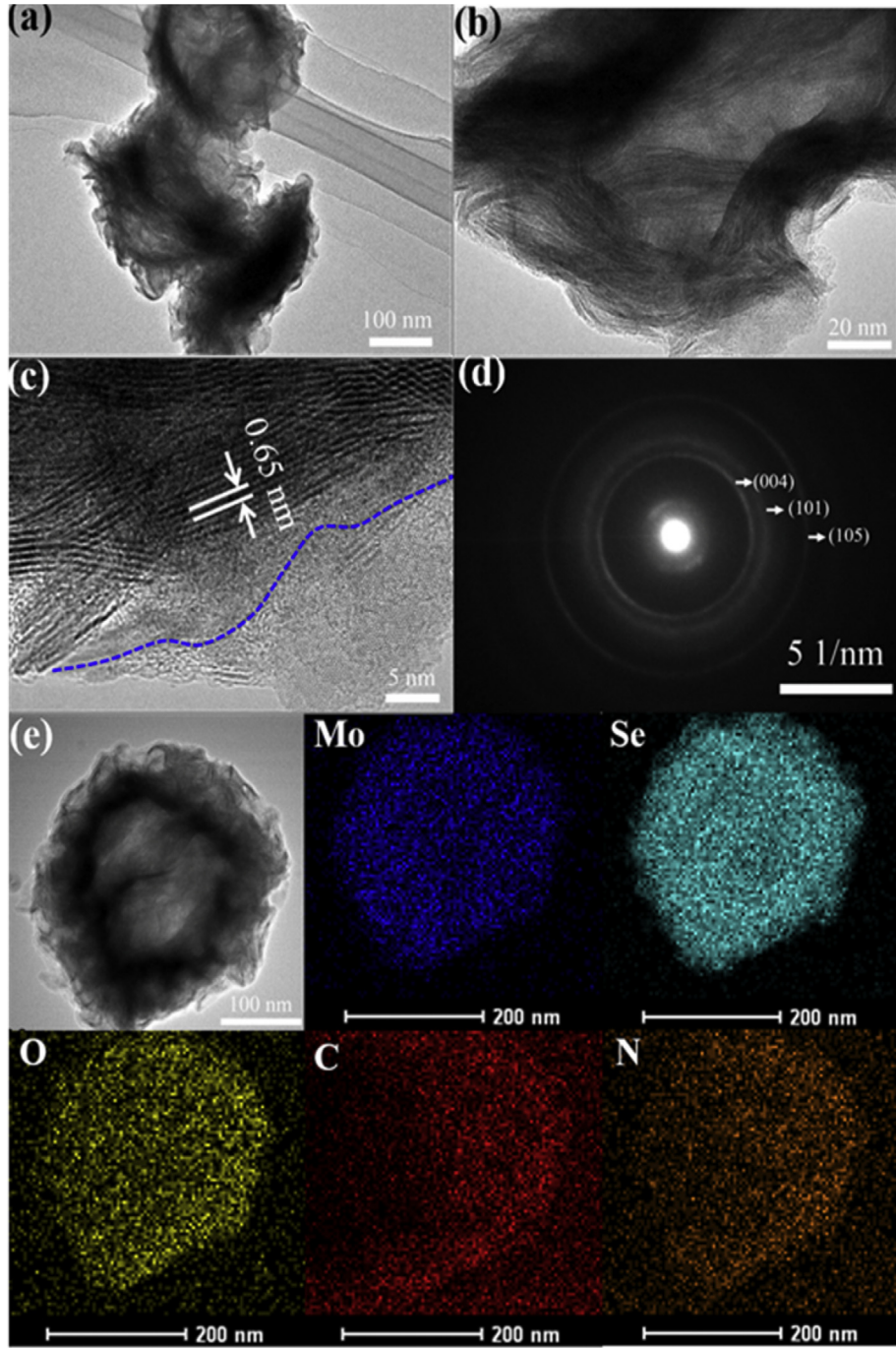


Fig. 6. (a, b) TEM, (c) HRTEM images, (d) SAED pattern and (e) EDX mapping of $\text{MoSe}_2/\text{MoO}_3$ composite.

Rate performance of the $\text{MoSe}_2/\text{MoO}_3$ composite and the MoSe_2 nanostructure anode were measured and compared in Fig. 8a. When cycling for 10 cycles at current densities of 0.1, 0.5, 1.0, 2.0, 5.0, 8.0 and 10.0 A g^{-1} , the $\text{MoSe}_2/\text{MoO}_3$ composite electrode shows discharge capacities of 567, 487, 458, 420, 366, 326 and 314 mAh g^{-1} , respectively. The corresponding capacities of the MoSe_2 anode are 395, 335, 317, 294, 249, 223 and 209 mAh g^{-1} , respectively. The capacity retention is as high as 55.4% when the current density increases from 0.1 to 10.0 A g^{-1} (100-fold increase), revealing excellent rate capability. Obviously, the $\text{MoSe}_2/\text{MoO}_3$ composite anode exhibits much higher capacities at each current density and better rate capacity retention (55.4%) than the pristine MoSe_2

anode which maintains a rate capacity retention of 52.9%. Both samples gradually increase to their initial capacities when the currents gradually decrease to 0.1 A g^{-1} , indicating good rate-cycling stability for the anodes in SIBs. Electrochemical impedance spectroscopy (EIS) measurements were carried out over the frequency range of 10 mHz – 100 kHz to investigate the electrochemical performance difference between $\text{MoSe}_2/\text{MoO}_3$ composite and the MoSe_2 nanostructure anodes. Typical Nyquist plots of the cells with the two samples are shown in Fig. 8b. All the plots exhibit a semicircle in the high-frequency region and a straight line in the low frequency region. The semicircle in the middle frequency range is attributed to the charge transfer resistance (R_{ct}), which

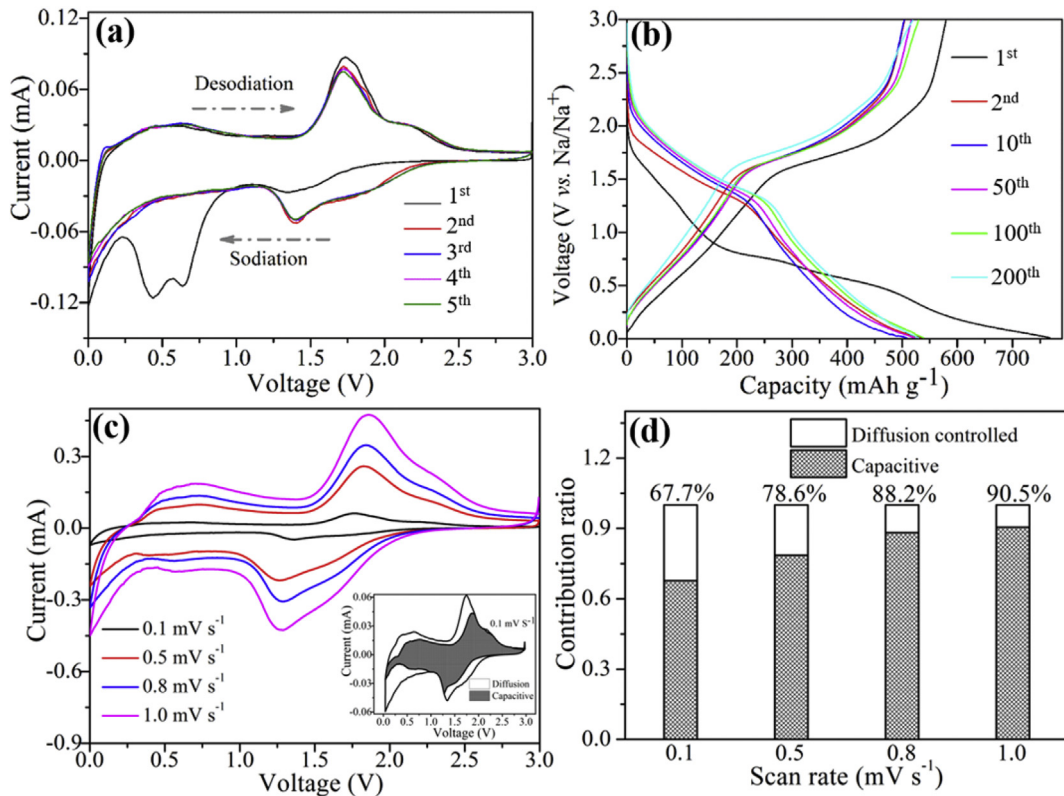


Fig. 7. (a) CV curves of the $\text{MoSe}_2/\text{MoO}_3$ composite anode at a scan rate of 0.1 mV s^{-1} for the initial five cycles over the voltage range of $0.0\text{--}3.0 \text{ V}$. (b) Typical discharge/charge curves of the $\text{MoSe}_2/\text{MoO}_3$ composite at the current density of 500 mA g^{-1} after active process in the first cycle at current of 50 mA g^{-1} . (c) CV curves at varying sweep rates for the $\text{MoSe}_2/\text{MoO}_3$ composite electrode; inset: capacitive (shade region) and diffusion-controlled charge storage contributions. (d) Contribution ratio of the capacitive and diffusion-controlled charges at different scan rates.

corresponds to the charge transfer through the electrode/electrolyte interface. The R_{ct} for $\text{MoSe}_2/\text{MoO}_3$ composite electrode is lower than that of the MoSe_2 electrode, as shown in Fig. 8b. The results indicated that the amorphous MoO_3 layer can effectively decrease the charge transfer resistance and thus facilitates charge-transfer in the SIBs because of the amorphous nature [53].

In order to demonstrate the effects of the oxidation treatment on the cycle stability, the cycling performance of the two samples was also compared at the current of 1000 mA g^{-1} (Fig. 8c). The MoSe_2 shows a second discharge capacity of 347 mAh g^{-1} , the capacities are mostly stable values in the initial 150 cycles and after which degrade continuously to 307 mAh g^{-1} at the 200th cycle, giving a capacity retention of 88.5%. For the $\text{MoSe}_2/\text{MoO}_3$ composite anode, it shows high specific discharge capacities and an outstanding cycling stability. It delivers a capacity of 485 mAh g^{-1} at the 200th cycle with capacity retention of 101.9%, in comparison to the capacity in the 2nd cycle. As previous studies, the increased capacity is caused by the pseudo-capacitive behavior, which can be affected when the electrolyte penetrates into the inner part of the nanostructures along with the cycling. The superior cycling stability can be proved by the EIS results as shown in Fig. 8d. For the fresh cell, the R_{ct} is estimated to be $\sim 400 \Omega$. And this value decreased to be $\sim 103 \Omega$ and $\sim 75 \Omega$ after 1-cycle and 10-cycles, respectively. The decreased R_{ct} values should be attributed to an active process, leading to the crystalline active materials into ultrafine nanocrystals during the electrochemical reaction process [54,55]. The cycling performance of the $\text{MoSe}_2/\text{MoO}_3$ composite

anode was further investigated at low current of 500 mA g^{-1} and high current of 2000 mA g^{-1} (Fig. 8e). At both currents, the cycling performance is impressive. The $\text{MoSe}_2/\text{MoO}_3$ composite anode can deliver stable capacities with high CE of about 99%, as shown in Fig. 8e. The CE shows a slight decrease trend due to the interfacial storage increase, which originate from progressive kinetic activation leading to more metal surface based on the fact of the slightly broken $\text{MoSe}_2/\text{MoO}_3$ nanostructures (Fig. S6.) and extra side reactions. After 200 cycles, the capacity retention can retain as high as 99.2% and 99.5% at currents of 500 and 2000 mA g^{-1} , respectively. The MoO_3 surface mainly plays a role as a coating layer to prevent selenium dissolution, and it subsequently improves the cycle performance.

4. Conclusions

In summary, we developed a facile method to prepare $\text{MoSe}_2/\text{MoO}_3$ heterogeneous nanostructures. As an anode material for SIBs, it shows higher specific capacities, higher rate capability and better cycling performance due to the amorphous MoO_3 layer. The discharge capacity is as high as 729 mAh g^{-1} at low current of 50 mA g^{-1} in the first cycle. For the rate performance, the capacity retention reaches up to 55.4% when the current density increases from low current of 0.1 A g^{-1} to high current of 10.0 A g^{-1} (100-fold increase). At currents of 500 , 1000 and 2000 mA g^{-1} , the capacities remain at high values of 529 , 485 and 453 mAh g^{-1} , respectively, at the 200th cycle with high capacity retentions. Amorphous MoO_3

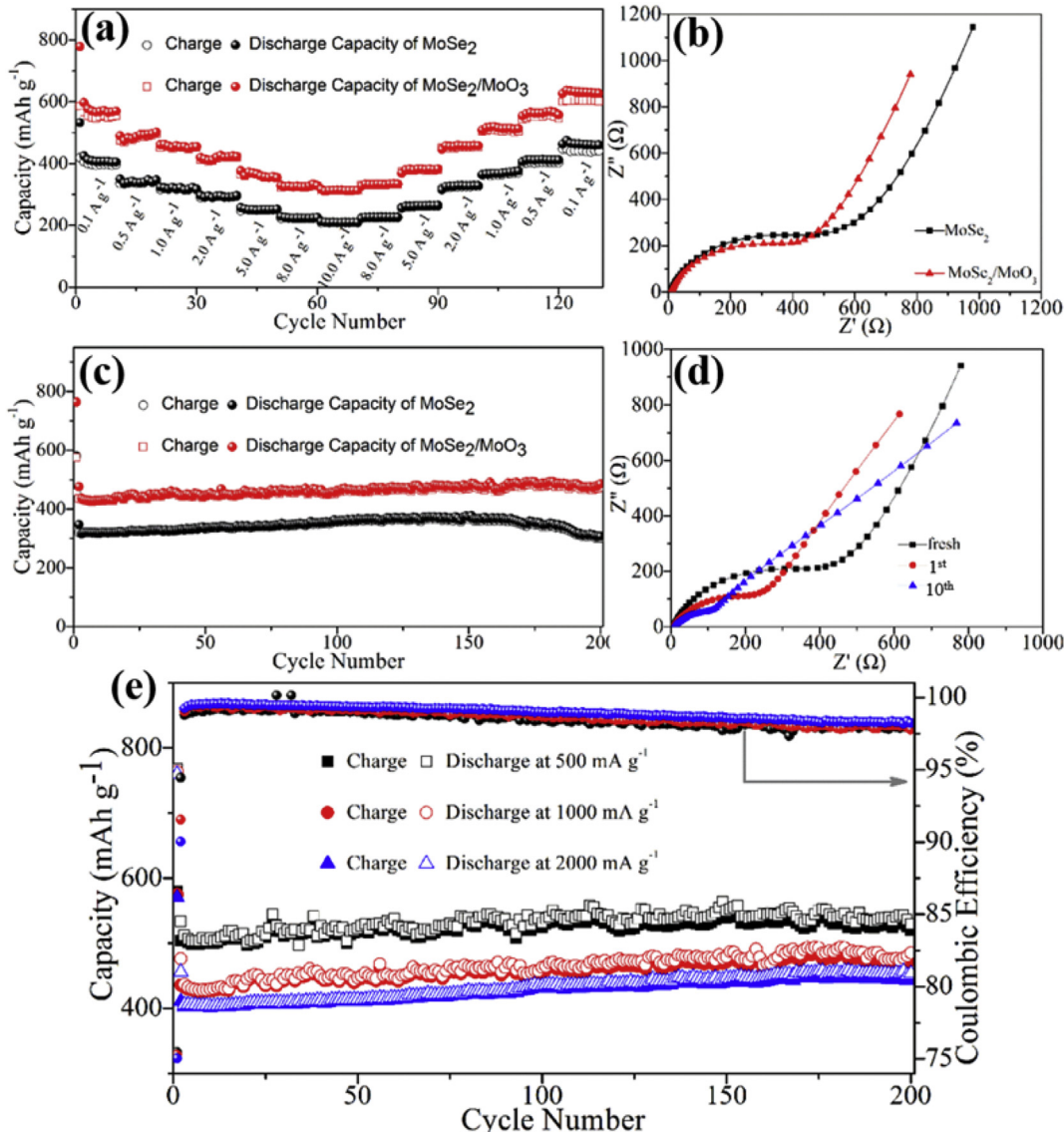


Fig. 8. (a) Rate capability and (b) Nyquist plots for MoSe₂ and MoSe₂/MoO₃ composite; (c) The cycling performance at current of 1000 mA g⁻¹ after the first low current activation cycle at current of 50 mA g⁻¹ for MoSe₂ and MoSe₂/MoO₃ composite; (d) Nyquist plots for MoSe₂/MoO₃ composite after different cycles; (e) The cycling performance at different current densities after the first low current activation cycle at current of 50 mA g⁻¹ for MoSe₂/MoO₃ composite electrode.

layer on the surface of the MoSe₂ is responsible for the enhanced electrochemical performance. It is believed that the high rate capacity and cycling stability of this MoSe₂/MoO₃ heterogeneous nanostructure will make it a promising anode candidate for high performance SIB applications.

Acknowledgements

This work was financially supported by the National Natural Science Foundation of China (NSFC Grant 21571187, 21501198, 51702366), Taishan Scholar Foundation (ts201511019), Natural Science Foundation of Shandong Province (ZR2017BB046) and the Fundamental Research Funds for the Central Universities (17CX02037A).

Appendix A. Supplementary data

Supplementary data related to this article can be found at

<https://doi.org/10.1016/j.jallcom.2018.02.037>.

References

- [1] W. Luo, F. Shen, C. Bommier, H. Zhu, X. Ji, L. Hu, Na-ion battery anodes: materials and electrochemistry, *Acc. Chem. Res.* 49 (2016) 231–240.
- [2] S.Y. Hong, Y. Kim, Y. Park, A. Choi, N.-S. Choic, K.T. Lee, Charge carriers in rechargeable batteries: Na ions vs. Li ions, *Energy Environ. Sci.* 6 (2013) 2067–2081.
- [3] S.P. Ong, V.L. Chevrier, G. Hautier, A. Jain, C. Moore, S. Kim, X. Ma, G. Ceder, Voltage, stability and diffusion barrier differences between sodium-ion and lithium-ion intercalation materials, *Energy Environ. Sci.* 4 (2011) 3680–3688.
- [4] Y.C. Liu, Y. Li, H.Y. Kang, T. Jin, L.F. Jiao, Design, synthesis, and energy-related applications of metal sulfides, *Mater. Horiz.* 3 (2016) 402–421.
- [5] B. Dunn, H. Kamath, J.-M. Tarascon, Electrical energy storage for the grid: a battery of choices, *Science* 334 (2011) 928–935.
- [6] V. Palomares, P. Serras, I. Villaluenga, K.B. Hueso, J. Carretero-González, T. Rojo, Na-ion batteries, recent advances and present challenges to become low cost energy storage systems, *Energy Environ. Sci.* 5 (2012) 5884–5901.
- [7] M.H. Han, E. Gonzalo, G. Singh, T. Rojo, A comprehensive review of sodium layered oxides: powerful cathodes for Na-ion batteries, *Energy Environ. Sci.* 8 (2015) 81–102.
- [8] W. Kang, Z. Zhang, P.-K. Lee, T.-W. Ng, W. Li, Y. Tang, W. Zhang, C.-S. Lee,

- D.Y.W. Yu, Copper substituted P2-type $\text{Na}_{0.67}\text{CuMn}_{1-x}\text{O}_2$: a stable high-power sodium-ion battery cathode, *J. Mater. Chem. A* 3 (2015) 22846–22852.
- [9] S.-W. Kim, D.-H. Seo, X. Ma, G. Ceder, K. Kang, Electrode materials for rechargeable sodium-ion batteries: potential alternatives to current lithium-ion batteries, *Adv. Energy Mater.* 2 (2012) 710–721.
- [10] L. Wang, Y. Lu, J. Liu, M. Xu, J. Cheng, D. Zhang, J.B. Goodenough, A superior low-cost cathode for a Na-ion battery, *Angew. Chem. Int. Ed.* 52 (2013) 1964–1967.
- [11] W. Kang, Y. Wang, Jun Xu, Recent progress in layered metal dichalcogenide nanostructures as electrodes for high-performance sodium-ion batteries, *J. Mater. Chem. A* 5 (2017) 7667–7690.
- [12] a) M.Q. Zhao, X. Xie, C.E. Ren, T. Makaryan, B. Anasori, G. Wang, Y. Gogotsi, Hollow MXene spheres and 3D macroporous MXene frameworks for Na-ion storage, *Adv. Mater.* 29 (2017), 1702410; b) Y. Kim, K.-H. Ha, S.M. Oh, K.T. Lee, High-capacity anode materials for sodium-ion batteries, *Chem. Eur. J.* 20 (2014) 11980–11992.
- [13] X. Hu, W. Zhang, X. Liu, Y. Mei, Y. Huang, Nanostructured Mo-based electrode materials for electrochemical energy storage, *Chem. Soc. Rev.* 44 (2015) 2376–2404.
- [14] Z. Hu, Z. Zhu, F. Cheng, K. Zhang, J. Wang, C. Chen, J. Chen, Pyrite FeS_2 for high-rate and long-life rechargeable sodium batteries, *Energy Environ. Sci.* 8 (2015) 1309–1316.
- [15] K. Zhang, M. Park, L. Zhou, G.-H. Lee, W. Li, Y.-M. Kang, Jun Chen, Urchin-like CoSe_2 as a high-performance anode material for sodium-ion batteries, *Adv. Funct. Mater.* 26 (2016) 6728–6735.
- [16] J. Zhao, L. Zhao, K. Chihara, S. Okada, J. Yamaki, S. Matsumoto, S. Kuze, K. Nakane, Electrochemical and thermal properties of hard carbon-type anodes for Na-ion batteries, *J. Power Sources* 244 (2013) 752–757.
- [17] K. Tang, L. Fu, R.J. White, L. Yu, M.-M. Titirici, M. Antonietti, J. Maier, Hollow carbon nanospheres with superior rate capability for sodium-based batteries, *Adv. Energy Mater.* 2 (2012) 873–877.
- [18] A. Ponrouch, A.R. Goñi, M. Rosa Palacín, High capacity hard carbon anodes for sodium ion batteries in additive free electrolyte, *Electrochim. Commun.* 27 (2013) 85–88.
- [19] Y. Xu, Y. Zhu, Y. Liu, C. Wang, Electrochemical performance of porous carbon/tin composite anodes for sodium-ion and lithium-ion batteries, *Adv. Energy Mater.* 3 (2013) 128–133.
- [20] L. Wu, X. Hu, J. Qian, F. Pei, F. Wu, R. Mao, X. Ai, H. Yang, Y. Cao, Sb-C nanofibers with long cycle life as an anode material for high-performance sodium-ion batteries, *Energy Environ. Sci.* 7 (2014) 323–328.
- [21] J. Sun, H.-W. Lee, M. Pasta, H. Yuan, G. Zheng, Y. Sun, Y. Li, Y. Cui, A phosphorene-graphene hybrid material as a high-capacity anode for sodium-ion batteries, *Nat. Nanotechnol.* 10 (2015) 980–985.
- [22] A. Rudola, K. Saravanan, C.W. Masona, P. Balaya, $\text{Na}_2\text{Ti}_3\text{O}_7$: an intercalation based anode for sodium-ion battery application, *J. Mater. Chem. A* 1 (2013) 2653–2662.
- [23] Z. Hong, M. Wei, T. Lan, G. Cao, Self-assembled nanoporous rutile TiO_2 mesocrystals with tunable morphologies for high rate lithium-ion batteries, *Nano Energy* 1 (2012) 466–471.
- [24] C. Wu, P. Kopold, P.A. van Aken, J. Maier, Y. Yu, High performance graphene/ Ni_2P hybrid anodes for lithium and sodium storage through 3D yolk-shell-like nanostructural design, *Adv. Mater.* 29 (2017), 1604015.
- [25] X. Ge, Z. Li, L. Yin, Metal-organic frameworks derived porous core/shell CoP@C polyhedrons anchored on 3D reduced graphene oxide networks as anode for sodium-ion battery, *Nano Energy* 32 (2017) 117–124.
- [26] J. Zhang, W. Kang, M. Jiang, Y. You, Y. Cao, T.-W. Ng, D.Y.W. Yu, C.-S. Lee, J. Xu, Conversion of 1T- MoSe_2 to 2H- $\text{MoS}_{2x}\text{Se}_{2-2x}$ mesoporous nanospheres for superior sodium storage performance, *Nanoscale* 9 (2017) 1484–1490.
- [27] X. Xie, Z. Ao, D. Su, J. Zhang, G. Wang, MoS_2 /graphene composite anodes with enhanced performance for sodium-ion batteries: the role of the two-dimensional heterointerface, *Adv. Funct. Mater.* 25 (2015) 1393–1403.
- [28] W. Kang, Y. Zhang, L. Fan, L. Zhang, F. Dai, R. Wang, D. Sun, Metal-organic framework derived porous hollow $\text{Co}_3\text{O}_4/\text{N-C}$ polyhedron composite with excellent energy storage capability, *ACS Appl. Mater. Interfaces* 9 (2017) 10602–10609.
- [29] G. Fang, J. Zhou, Y. Cai, S. Liu, X. Tan, A. Pan, S. Liang, Metal-organic framework-templated two-dimensional hybrid bimetallic metal oxides with enhanced lithium/sodium storage capability, *J. Mater. Chem. A* 5 (2017) 13983–13993.
- [30] L. Lia, S. Peng, N. Bucherd, H.-Y. Chen, N. Shen, A. Nagasubramaniand, E. Eldho, S. Hartung, S. Ramakrishna, M. Srinivasan, Large-scale synthesis of highly uniform Fe_{1-x}S nanostructures as a high-rate anode for sodium ion batteries, *Nano Energy* 37 (2017) 81–89.
- [31] G.D. Park, J.S. Cho, Y.C. Kang, Sodium-ion storage properties of nickel sulfide hollow nanospheres/reduced graphene oxide composite powders prepared by a spray drying process and the nanoscale Kirkendall effect, *Nanoscale* 7 (2015) 16781–16788.
- [32] S.Z. Butler, S.M. Hollen, L. Cao, Y. Cui, J.A. Gupta, H.R. Gutierrez, T.F. Heinz, S.S. Hong, J. Huang, A.F. Ismach, E. Johnston-Halperin, M. Kuno, V.V. Plashnitsa, R.D. Robinson, R.S. Ruoff, S. Salahuddin, J. Shan, L. Shi, M.G. Spencer, M. Terrones, W. Windl, J.E. Goldberger, Progress, challenges, and opportunities in two-dimensional materials beyond graphene, *ACS Nano* 7 (2013) 2898–2926.
- [33] X. Xie, T. Makaryan, M. Zhao, K.L. Van Aken, Y. Gogotsi, G. Wang, MoS_2 nanosheets vertically aligned on carbon paper: a freestanding electrode for highly reversible sodium-ion batteries, *Adv. Energy Mater.* 6 (2016), 1502161.
- [34] H. Wang, H. Yuan, S.S. Hong, Y. Li, Y. Cui, Physical and chemical tuning of two-dimensional transition metal dichalcogenides, *Chem. Soc. Rev.* 44 (2015) 2664–2680.
- [35] H. Wang, X. Lan, D. Jiang, Y. Zhang, H. Zhong, Z. Zhang, Y. Jiang, Sodium storage and transport properties in pyrolysis synthesized MoSe_2 nanoplates for high performance sodium-ion batteries, *J. Power Sources* 283 (2015) 187–194.
- [36] X. Yang, Z. Zhang, Y. Fu, Q. Li, Porous hollow carbon spheres decorated with molybdenum diselenide nanosheets as anodes for highly reversible lithium and sodium storage, *Nanoscale* 7 (2015) 10198–10203.
- [37] S.H. Choi, Y.C. Kang, Fullerene-like MoSe_2 nanoparticles-embedded CNT balls with excellent structural stability for highly reversible sodium-ion storage, *Nanoscale* 8 (2016) 4209–4216.
- [38] Z. Zhang, X. Yang, Y. Fu, K. Du, Ultrathin molybdenum diselenide nanosheets anchored on multi-walled carbon nanotubes as anode composites for high performance sodium-ion batteries, *J. Power Sources* 296 (2015) 2–9.
- [39] D. Xie, W. Tang, Y. Wang, X. Xia, Y. Zhong, D. Zhou, D. Wang, X. Wang, J. Tu, Facile fabrication of integrated three-dimensional C- MoSe_2 /reduced graphene oxide composite with enhanced performance for sodium storage, *Nano Res.* 9 (2016) 1618–1629.
- [40] Y.N. Ko, S.H. Choi, S.B. Parkc, Y.C. Kang, Hierarchical MoSe_2 yolk–shell microspheres with superior Na-ion storage properties, *Nanoscale* 6 (2014) 10511–10515.
- [41] K. Mi, S. Chen, B. Xi, S. Kai, Y. Jiang, J. Feng, Y. Qian, S. Xiong, Sole chemical confinement of polysulfides on nonporous nitrogen/oxygen dual-doped carbon at the kilogram scale for lithium-sulfur batteries, *Adv. Funct. Mater.* 27 (2017), 1604265.
- [42] J. Zhang, Y. Shi, Y. Ding, L. Peng, W. Zhang, G. Yu, A Conductive molecular framework derived $\text{Li}_2\text{S}/\text{N}$, P-codoped carbon cathode for advanced lithium-sulfur batteries, *Adv. Energy Mater.* 7 (2017), 1602876.
- [43] Z. Jian, S. Hwang, Z. Li, A.S. Hernandez, X. Wang, Z. Xing, D. Su, X. Ji, Hard-soft composite carbon as a long-cycling and high-rate anode for potassium-ion batteries, *Adv. Funct. Mater.* 27 (2017), 1700324.
- [44] J. Zhou, T. Qian, N. Xu, M. Wang, X. Ni, X. Liu, X. Shen, C. Yan, Batteries: selenium-doped cathodes for lithium-organosulfur batteries with greatly improved volumetric capacity and coulombic efficiency, *Adv. Mater.* 29 (2017), 1701294.
- [45] J. Ding, H. Zhou, H. Zhang, T. Stephenson, Z. Li, D. Karpuzovc, D. Mitlin, Exceptional energy and new insight with a sodium–selenium battery based on a carbon nanosheet cathode and a pseudographite anode, *Energy Environ. Sci.* 10 (2017) 153–165.
- [46] B. Ahmed, D.H. Anjum, M.N. Hedhili, H.N. Alshareef, Mechanistic insight into the stability of HfO_2 -coated MoS_2 nanosheet anodes for sodium ion batteries, *Small* 11 (2015) 4341–4350.
- [47] W.-H. Ryu, H. Wilson, S. Sohn, J. Li, X. Tong, E. Shaulsky, J. Schroers, M. Elimelech, A.D. Taylor, Heterogeneous WS_x/WO_3 thorn-bush nanofiber electrodes for sodium-ion batteries, *ACS Nano* 10 (2016) 3257–3266.
- [48] R.K. Sharma, G.B. Reddy, Synthesis and characterization of $\alpha\text{-MoO}_3$ microspheres packed with nanoflakes, *J. Phys. D Appl. Phys.* 47 (2014), 065305.
- [49] X. Wang, Y.P. Zhang, Z.Q. Chen, Effect of MoO_3 constituents on the growth of MoS_2 nanosheets by chemical vapor deposition, *Mater. Res. Express* 3 (2016), 065014.
- [50] S. Vishwanath, X. Liu, S. Rouvimov, P. C Mende, A. Azcatl, S. McDonnell, R. M Wallace, R.M. Feenstra, J.K. Furdyna, D. Jena, H.G. Xing, Comprehensive structural and optical characterization of MBE grown MoSe_2 on graphite, CaF_2 and graphene, *2D Mater.* 2 (2015), 024007.
- [51] S. Hariharan, K. Saravanan, P. Balaya, $\alpha\text{-MoO}_3$: a high performance anode material for sodium-ion batteries, *Electrochim. Commun.* 31 (2013) 5–9.
- [52] X. Xie, M.Q. Zhao, B. Anasori, K. Maleski, C.E. Ren, J. Li, B.W. Byles, E. Pomerantseva, G. Wang, Y. Gogotsi, Porous heterostructured MXene/carbon nanotube composite paper with high volumetric capacity for sodium-based energy storage devices, *Nano Energy* 26 (2016) 513–523.
- [53] J. Guo, Q. Liu, C. Wang, M.R. Zachariah, Interdispersed amorphous MnO_x -carbon nanocomposites with superior electrochemical performance as lithium-storage material, *Adv. Funct. Mater.* 22 (2012) 803–811.
- [54] Q. Wang, W. Zhang, C. Guo, Y. Liu, C. Wang, Z. Guo, In situ construction of 3D interconnected $\text{FeS}@\text{Fe}_3\text{C}$ @graphitic carbon networks for high-performance sodium-ion batteries, *Adv. Funct. Mater.* 27 (2017), 1703390.
- [55] J.S. Cho, S.Y. Lee, Y.C. Kang, First introduction of NiSe_2 to anode material for sodium-ion batteries: a hybrid of graphene-wrapped NiSe_2/C porous nanofiber, *Sci. Rep.* 6 (2016), 23338.